

## 13. Topological Considerations in Fluid Mechanics Measurements

The vector field variables of interest in experimental fluid mechanics include velocity, vorticity and wall shear stress. Additional vector fields of interest include the gradients of pressure and temperature. Each of these is subject to the constraints that can be placed on the isolated singular points (vector magnitude = 0) of the vector field that is projected onto a surface of interest. Identifying the relevant surfaces for a given flow and establishing, for a given identified surface, an a priori constraint on the isolated singular points of the relevant vector field, can provide experimentalists with a powerful diagnostic tool.

13.1	<b>A Companion Document</b> .....	909
13.2	<b>Utilization of Topological Considerations for Flow Field Analyses</b> .....	910
13.2.1	A <i>Tabbed Jet</i> .....	910
13.2.2	A Conical Flame Holder Geometry ...	911
13.2.3	Flow Past a Small-Aspect-Ratio <i>Protruding Cylinder</i> .....	912
13.2.4	A Vortex Ring-Wall Interaction .....	913
13.2.5	An Annular Jet .....	915
13.2.6	Summary .....	917
	<b>References</b> .....	918

It is the purpose of this chapter of the handbook to enable the reader to utilize this diagnostic tool for any flow field of interest.

### 13.1 A Companion Document

The present author has published an article [13.1] that provides a detailed description of the steps that are required to develop and to utilize this diagnostic tool. It is expected that the interested reader will consult that reference for the supporting material that undergirds this presentation. The following items, whose focus is to develop the reader's capability to utilize this diagnostic tool, must first provide a synopsis of that more complete presentation. The following section then provides examples of the use of this diagnostic tool in the service of flow field analyses.

If the surface of interest is overlaid on a physical (no-slip) body, then the isolated singular points will satisfy the relationship

$$\chi_{\text{surface}} = \sum N - \sum S \quad (13.1)$$

where  $\chi$  is the Euler characteristic of the selected surface. The term *no-slip surface* was introduced by Perry and Chong [13.2] and [13.3] for such surfaces. Alternatively, [13.1] utilizes the term *body fitted* to emphasize the relationship of the diagnostic surface to the object of interest.

Given that any surface can be formed from a sphere into which  $N$  holes have been *punched* and/or  $M$  handles

have been attached, as described in [13.1], the  $\chi$  value for the surface can be established as

$$\chi_{\text{surface}} = 2 - \sum \text{holes} - 2 \sum \text{handles} . \quad (13.2)$$

The connection between (13.1) and (13.2) is established by the condition that the Euler characteristic for a surface is equal to the sum of the indices for that surface and recognizing that a node ( $N$ ) is represented by an index of +1 and a saddle ( $S$ ) by an index of -1. [13.1] provides the identification technique to identify a node and a saddle as well as specific examples that clarify the definition of the *surfaces* to be analyzed via (13.1) and (13.2). Stated succinctly, the identification technique involves a unit vector that is, at every location of its base point, aligned with the vector under consideration. The base point of this unit vector is placed on a circle that surrounds the location of interest. The base is then caused to rotate in a clockwise direction around the circle.

- If the unit vector rotates clockwise during the circuit, then a *net* node is enclosed by the circle.
- If the unit vector rotates counterclockwise, then a *net* saddle is enclosed by the circle.

- If there is no net rotation, then there is no *net* singular point within the circle.

If a surface is selected that exists within a flow field (either fully or with boundaries that touch a physical surface), then (13.1) is generalized to

$$\chi_{\text{surface}} = 2 \sum N + \sum N' - 2 \sum S - \sum S'. \quad (13.3)$$

Such a surface is most easily visualized by considering an inflated balloon, gripping the balloon along *seams* that are contours in space that are tangent to the vectors, evacuating the balloon such that it collapses to a *two-sided (perhaps warped) plane*. A flattened *pancake* or *crepe* is a good simile for this surface. One

or more holes may be added where the fluid can flow onto or leave the surface. (An important constraint for the vector field at a hole is: the vector field direction must be uniformly inward or outward at all points along the contour defined by the hole.) In this description, a singular point on the *seam* of the surface will appear once in the summation and, following Hunt et al. [13.4], the singular points on a seam are termed half-nodes or half-saddles. Singular points that are interior to the seams are *full nodes* or *full saddles* and these are counted twice in the summation as shown in (13.3). Specifically, they are counted once for each side of the collapsed sphere.

Numerous examples are provided in [13.1] as well as in the following section to clarify these concepts.

## 13.2 Utilization of Topological Considerations for Flow Field Analyses

In addition to the illustrative examples of the basic concepts, only two flows: *Koster and Müller* [13.6] plus *Zimmermann et al.* [13.7] and *Ruderich and Fernholz* [13.8] are considered in detail in [13.1]. The importance of the first group and the second reference is that: (i) the completeness of the inferred flow pattern was confirmed in the former, and (ii) the published flow pattern was corrected in the latter. Specifically, by applying the topological rule to different surfaces in each case, it was possible to extend the understanding of each flow beyond that provided in the original reference. The essential contribution of this Handbook section is to provide further examples that will aid the reader in the effective use of this diagnostic tool.

### 13.2.1 A Tabbed Jet

#### Velocity Measurements in the Tab's Wake

The addition of triangular tabs at the exit plane of a jet is an effective means of promoting rapid mixing between the jet fluid and the ambient fluid. Initial studies of the tabbed jet: *Bradbury and Khadem* [13.9], *Zaman, et al.* [13.10], and *Reeder and Samimy* [13.11], were extended by *Bohl and Foss* [13.12] with the addition of secondary tabs at the sides of the primary tab. Figure 13.1 shows the geometry for the primary plus secondary tabs. The Figures in this Section are taken from the MS thesis of *Bohl* [13.5]. (See *Bohl and Foss* [13.12] for the *open literature* source of the same information.)

The source of the strong streamwise vortex motions (that result in the near field mixing) was identified as the surface pressure distribution forward of the primary tab. The secondary tabs serve to promote this mixing by enhancing the outward trajectory of the streamwise vortex motions beyond the exit plane of the jet.

An X-array of hot-wire sensors was positioned at a regular array of  $y$  and  $z$  locations at two different downstream locations. Two time series measurements ( $u, v$ ) and ( $u, w$ ) were obtained over this grid of points. Using these data, the time-averaged ( $\bar{v}$ ,  $\bar{w}$ ) components of the velocity vector allowed the projected streamlines, in the planes of constant  $x$ , to be defined. A representative streamline pattern is shown in Fig. 13.2a.

The index identification technique, [13.1] and Sect. 13.1, was used to establish the indicated nodes (13.2) and saddles (13.2) that can be identified in the

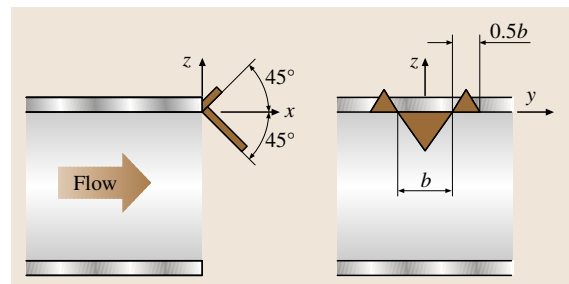
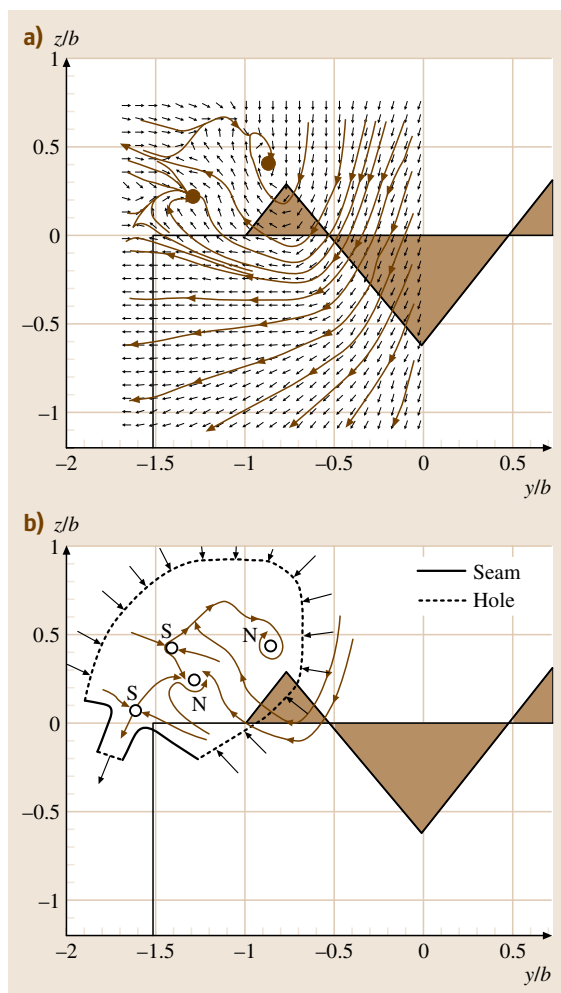


Fig. 13.1 Primary and secondary tabs (after Bohl [13.5])



**Fig. 13.2a,b** Streamlines in the “collapsed surface” at  $x/b = 1.2$  for the geometry of Fig. 13.1. **(a)** Measured velocity field with inferred streamlines. **(b)** Seams (solid) and holes (dashed) to analyze the flow of **(a)**

measured field. These singular points exist on the surface of the *collapsed sphere with two holes* that is also identified in this figure. Given that the collapsed sphere has two holes and given the two nodes and the two saddles, (13.3) is satisfied by the information in Fig. 13.2b. The self-consistency of these identifications gives confidence to these inferences from the experimental data.

#### Observations on the Approach and the Tab Surfaces

Surface streaking observations on the approach surface, plus the inclined primary tab were also made. This image

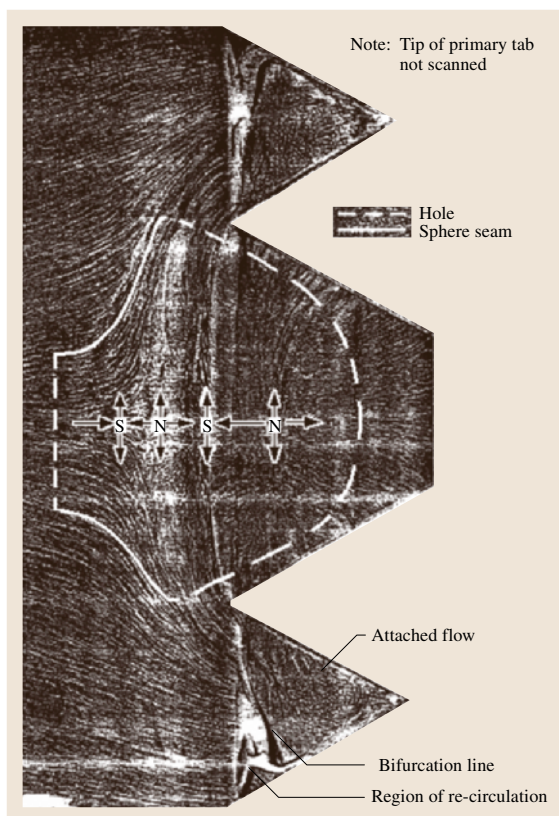


**Fig. 13.3** Surface streak image (lampblack and kerosene) of the approach surface and the primary tab. The overlaid dashed white lines are the entry and exit holes. The seams (solid lines) are aligned with the limiting streamlines.

is shown in Fig. 13.3. A collapsed sphere can be identified (as shown in Fig. 13.3) with an entry and an exit hole. The two nodes and the two saddles contained within these borders are compatible with the sphere plus the two holes of Fig. 13.3. Note that a single surface formed as a disc to cover the same area could not be used since the exposed edge would not provide a unidirectional flow. (A disc is formed by adding one hole to a sphere and *flattening* the remainder of the original surface.)

A side view of the flow field's center plane can be inferred from the surface singular points (Fig. 13.4). This image, again a collapsed sphere with two holes, involves two nodes and four half-saddles that, in summation, are compatible with the  $\chi = 0$  condition for (13.3). The contribution of the topological considerations is to infer the presence of the surface nodes in Fig. 13.3 as well as the nodes in Fig. 13.4 given the easily identified saddles of Fig. 13.3. The use of two surfaces to confidently

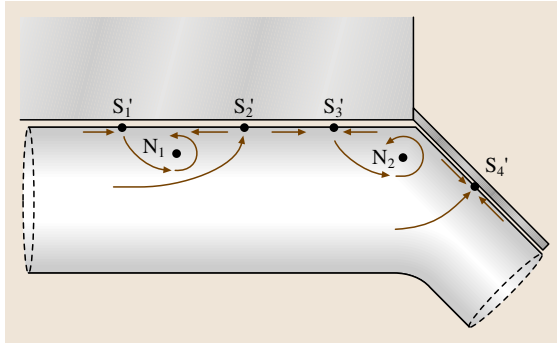


**Fig. 13.4** A collapsed sphere in the center plane of the tabbed jet flow

characterize one flow field is the rule rather than an exception.

### 13.2.2 A Conical Flame Holder Geometry

The masters thesis work of *Holland* [13.13] examined the external flow past an axisymmetric flame holder geometry; see Fig. 13.5a for an elevation view of this axisymmetric configuration. The purpose of this investigation was to establish the baseline flow field for computation fluid dynamics (CFD) verification. The actual flame holder would involve a central tube that delivers fuel into the airstream. The flow field associated with Fig. 13.5a can be modeled with a body fitted surface as a sphere with one hole. A *sock*, which extends from the base of the conical section to the upper dashed line in Fig. 13.5a, defines this body fitted surface. Figure 13.5b identifies the one node ( $N_1$ ) that satisfies the rule for this body fitted surface. There are, near the perimeter of the cone, two rings of singular points which do not contribute to the topology of this body fitted surface since they are not isolated. Their diameters  $d_2$  and  $d_3$  correspond to the  $S'_2$  and  $S'_3$  identifications of the collapsed surface singular points shown in Fig. 13.5c.

A collapsed-sphere surface, that can also be used to analyze this flow, is shown in Fig. 13.5a as the dashed line that includes the inlet and exiting flows. This surface has three holes. The dual ring of singular points is now involved in the counting as shown in Fig. 13.5c. The rule is satisfied as

$$\begin{aligned}\chi &= 2 - 3 \text{ holes} = -1 \\ &= 2 \sum N + \sum N' - 2 \sum S - \sum S' \\ &= 2(4) + 0 - 2(1) - 7.\end{aligned}\quad (13.4)$$

It is noteworthy that the interior  $S'_2$ , near the perimeter, which represents a separation location, was clearly

evident in the surface streaking image. The middle half-saddle  $S'_3$  (which represents an attachment location) was quite difficult to discern. As shown in Fig. 13.5c, this middle  $S'$  location is clearly required to provide a smoothly continuous vector field.

It is left as an *interesting exercise* to consider the vector field in the presence of an exiting fuel flow which would replace the singular point  $S_1$  in Fig. 13.5b. (Four holes lead to  $\chi = -2 = 2(4) + 0 - 2(2) - 6$ .)

### 13.2.3 Flow Past a Small-Aspect-Ratio Protruding Cylinder

*Summer* et al. [13.14] examined the wake region of a flow past cylinders of length ( $L$ ) and diameter  $D$  with  $L/D = 9, 7, 5$  and  $3$ . The cylinders' axes were perpendicular to the surface to which they were attached. A schematic representation of this experiment is shown in Fig. 13.6.

Two representative images of the streamwise vorticity magnitudes, inferred from the  $(v, w)$  components as obtained from seven hole probe measurements, are shown in Fig. 13.7a,b for the  $L/D = 5$  and  $L/D = 3$  cases, respectively. It is apparent that the smaller aspect ratio case does not show the lower pair of streamwise vortex motions that are evident in Fig. 13.7a.

Figures 13.8a,b show the corresponding surfaces that can be used to represent these two flows. Namely, a sphere with one hole would form a disc which, when folded (like a taco shell) forms a two-sided semicircular disc. The straight portion of the folded disc is placed on the surface (that supports the cylinder) at the  $x$ -location of the measurements. The circular perimeter of the folded disc, which represents the hole, will experience an inflow as shown by the swirling flow pattern of the four vortex motions Fig. 13.7a and the two vortex motions Fig. 13.7b. (Alternatively, one can create the equivalent semicircular pattern with a collapsed sphere followed by opening a hole along the circumference of the semicircle.) The vectors at the perimeter (above the plate) are inward, in agreement with the spatially averaged condition,  $\partial u / \partial x > 0$ , for the plane of constant  $x$  in the wake.

The  $L/D = 5$  vector field of Fig. 13.8a must be supplemented with inferred saddle points at lateral positions beyond the measurement domain. These are required to ensure a uniform inflow at the lateral boundary. With these additions, the topological constraint is satisfied as

$$\begin{aligned}\chi &= \chi_{\text{sphere}} + 1 \text{ hole} = 1 \\ &= 2 \sum N + \sum N' - 2 \sum S - \sum S' \\ &= 2(4) + 0 - 2(3) - 1 = 1.\end{aligned}\quad (13.5)$$

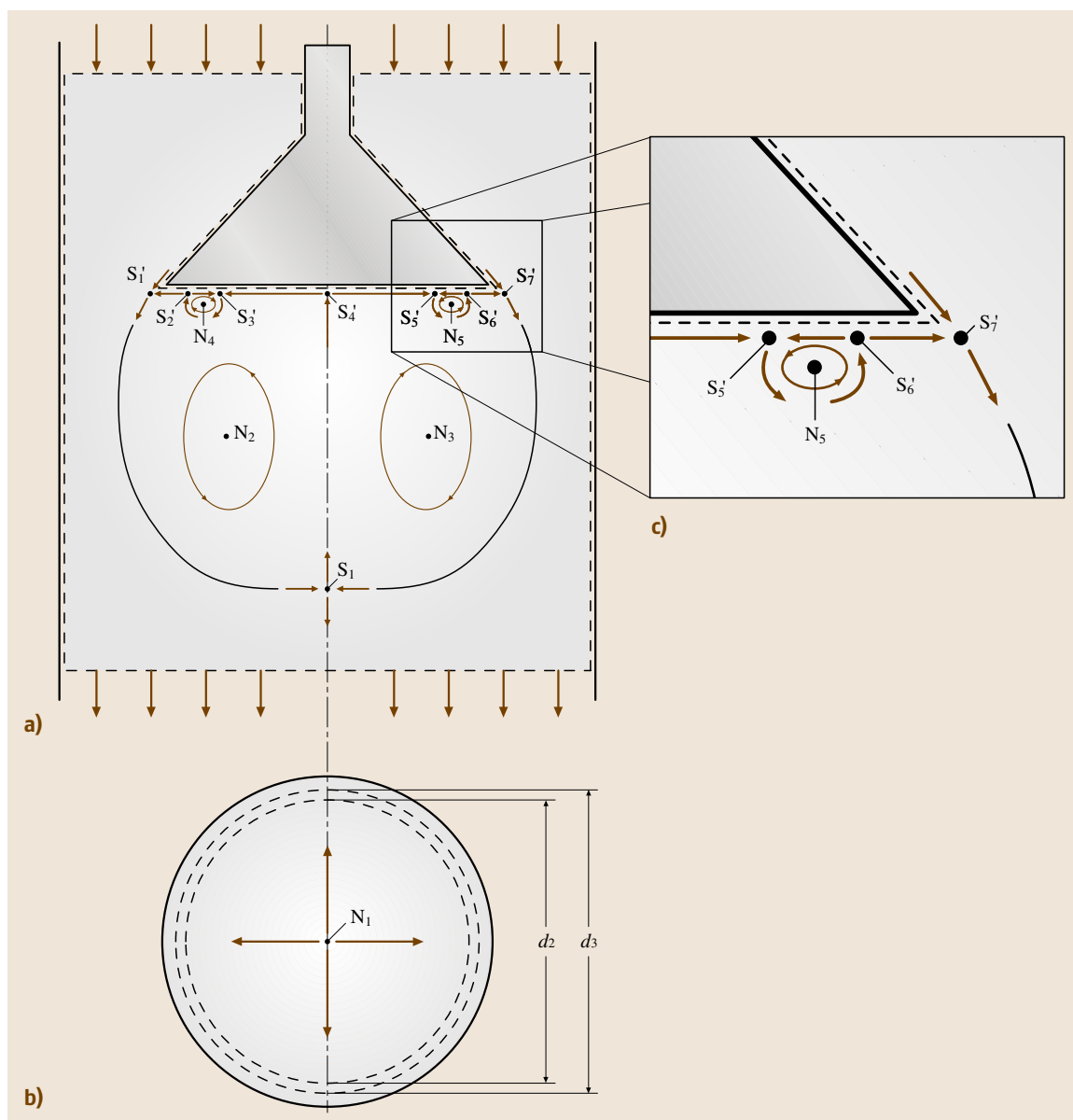


**Fig. 13.5a–c** A conical flame holder geometry. **(a)** Elevation view with a collapsed sphere at the midplane. **(b)** Bottom view with separation/reattachment rings. **(c)** Elevation view detail with separation/reattachment half-saddles

In contrast, the  $L/D = 3$  flow field involves two streamwise vortex motions:  $2N$  and three half-saddles at the lower boundary. The constraint is again satisfied as

$$\begin{aligned}\chi &= 1 = 2 \sum N + \sum N' - 2 \sum S - \sum S' \\ &= 2(2) + 0 - 0 - 3 = 1\end{aligned}\quad (13.6)$$

### 13.2.4 A Vortex Ring–Wall Interaction

Gendrich et al. [13.15] utilized molecular tagging velocimetry (see Sect. 5.4 of this Handbook) to examine the kinematics of a vortex ring that impinges on a planar surface; see Fig. 13.9 for a schematic representation of this experiment. The associated velocity field, at an



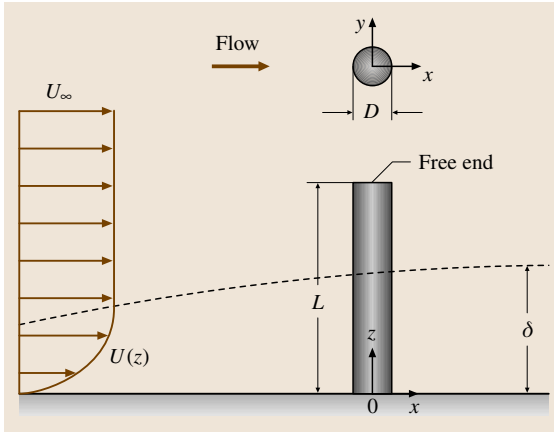


**Fig. 13.6** The experiment of Summer et al. [13.14]

instant, is presented in Fig. 13.10. This flow shows the intriguing characteristic that, following the outward spread of the ring on the surface, a rebound effect is present in which perimeter fluid is swept back toward the ring's axis and lifted off the impact surface. A companion flow: two rings that collide with a common axis was studied by Chu et al. [13.16]. The present analysis would also be related to that flow.

The body fitted analysis for this flow is quite simple: a sphere with one hole forms a disc on the surface and the centered stagnation point describes the single node. The disc, a sphere with one hole (hence,  $\chi = 1$ ), then satisfies the topological rule for both the outward, as well as the subsequent inward, flow at the disc's perimeter.

A mid-plane surface that contains the stagnation streamline provides a more interesting indication of this flow's topology. Using the domain defined by the

contour in Fig. 13.11a, the surface can be described as a collapsed sphere plus three holes. That is, the  $\chi$  value for Fig. 13.11a is  $-1$ . The axisymmetric nature of the vortex ring permits the streamlines, around the vortex core, to be drawn as closed contours. Seam 1, which follows this contour below the vortex, separates the inflow hole from the outflow holes. The centered stagnation point represents a half-saddle and, since the nodes of the ring vortex are excluded, the half-saddle satisfies the topological constraint as

$$\begin{aligned}\chi &= -1 = 2 \sum N + \sum N' - 2 \sum S - \sum S' \\ &= 0 + 0 - 0 - 1.\end{aligned}\quad (13.7)$$

Note that the  $S' - N - S'$  pattern of the separation and reattachment, if it were included in the contour, would be self-canceling.

The instructive aspect of this example derives from the identification of seam 2 and the following considerations Fig. 13.11b.

The collapsed surface for seam 2 now encloses the node that is represented by the vortex motion and this implies the presence of two half-saddles to cancel the

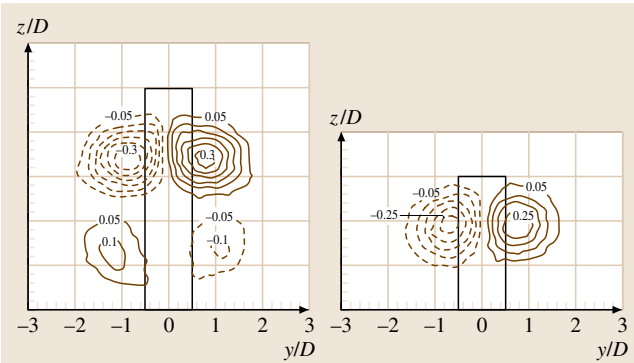


**Fig. 13.7a,b** The observed  $x = 6D$  plane streamlines for the flow of Fig. 13.6. (a)  $L/D = 5$ ; (b)  $L/D = 3$ . (After Summer et al. [13.14])

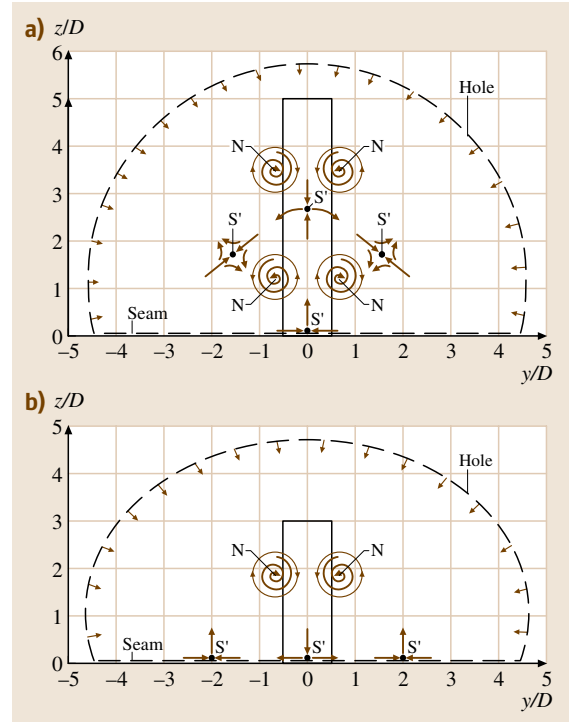


**Fig. 13.8a,b** Topological analyses for the flows of Fig. 13.7 (a)  $L/D = 5$ ; (b)  $L/D = 3$

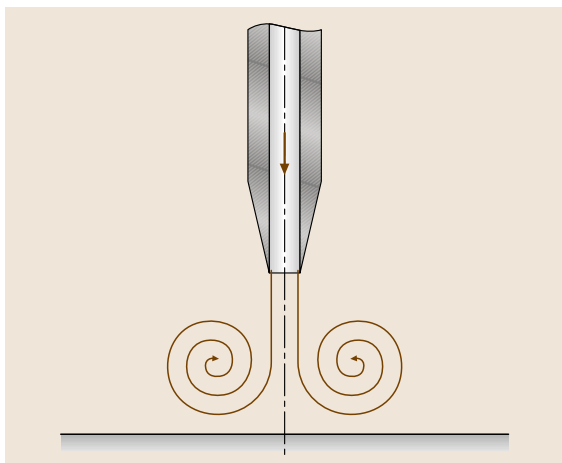


**Fig. 13.9** Vortex ring–wall interaction, a schematic representation of the experiment

contribution of the node. However, in a planar representation, as viewed in the plane normal to the impact plate, it appears that the vector field is *as continuous*, where seam 2 intersects the holes as it is for seam 1.

To understand why there must be a half-saddle at the intersection of the inlet hole and the streamline that covers the vortex motion (see point P on Fig. 13.11b), whereas there is no half-saddle at point P for Fig. 13.11a, one can visualize the *collapsed surface* as being flattened at point P as shown in Fig. 13.12a,b. In these views, it is apparent that a half-saddle must be present at point P for the seam 2 case (Fig. 13.12b). A similar *flattening* at Q will also reveal a half-saddle for the seam 2 condition.

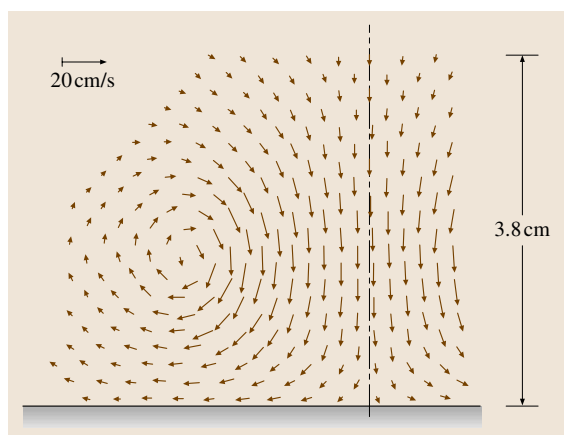


**Fig. 13.10** A representative instantaneous velocity field from the experiment of Fig. 13.9. Courtesy of M. M. Koochesfahani [13.17]

In contrast, a similar flattening for these same locations with seam 1 Fig. 13.12a would reveal no singular points at P and Q.

Hence, for the surface of seam 2, the rule is satisfied as:

$$\begin{aligned}\chi &= 2 \sum N + \sum N' - 2 \sum S - \sum S' \\ &= 2(2) + 0 - 0 - 5 \\ &= -1.\end{aligned}\quad (13.8)$$

### 13.2.5 An Annular Jet

Foss et al. [13.18] examined the velocity field in an annular jet formed by supporting a *streamlined plug* in the delivery tube of a round jet. The support was a cross-member attached to the perimeter of the delivery tube. The relevant features of the geometry for this flow are shown in Fig. 13.13.

The time-average separated, recirculating flow downwind from the plug is strongly three-dimensional as a result of the cross member. The present considerations will only address the vector field in a centered plane that is perpendicular to the cross-member. Particle image velocimetry (PIV) has been used to obtain 1000 images of the flow field downstream of the plug. Figure 13.14 presents the streamlines of the time-averaged field.

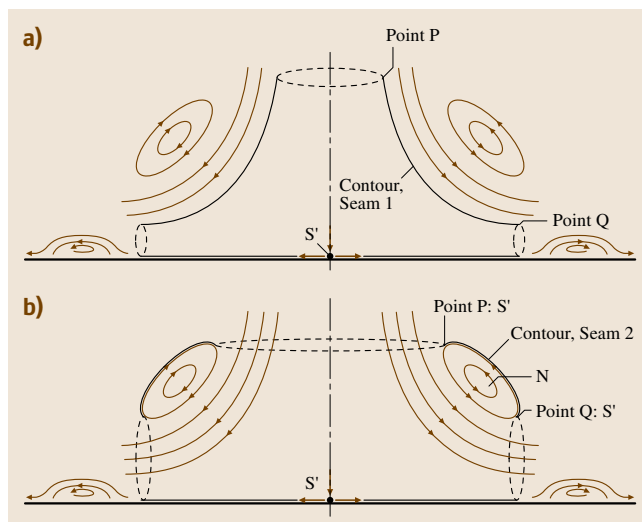


**Fig. 13.11a,b** The collapsed sphere plus two holes to describe the velocity field of Fig. 13.10. (a) A surface that excludes the right half-plane vortex (seam 1). (b) A surface that includes the right half-plane vortex (seam 2)

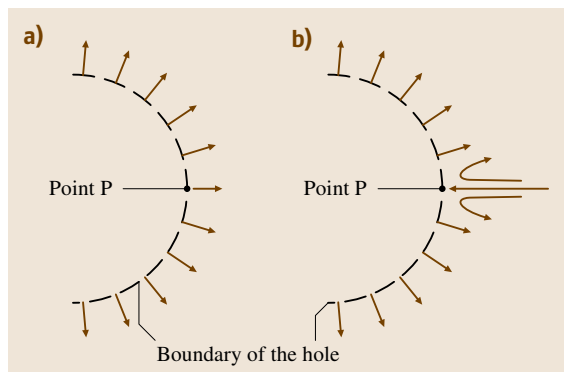


**Fig. 13.12a,b** A clarification of the absence/presence of a 1/2-saddle at point P in Fig. 13.11 for the surfaces of Fig. 13.11. (a) Absence of a half-saddle at point P for the seam 1 condition. (b) Presence of a half-saddle at point P for the seam 2 condition

Figure 13.15 provides a *skeleton* image of the relevant features (singular points) shown in Fig. 13.14 plus those associated with the plug itself. It also shows the domain for the topological analysis. Specifically, this collapsed sphere with two holes and one handle has an Euler characteristic of  $-2$ , which is satisfied as

$$\begin{aligned}\chi = -2 &= 2 \sum N + \sum N' - 2 \sum S - \sum S' \\ &= 2(3) + 0 - 2(2) - 4.\end{aligned}\quad (13.9)$$

It is noteworthy that  $S'_1$ ,  $S'_2$  and  $S'_3$  must be logically inferred since the PIV image cannot extend to

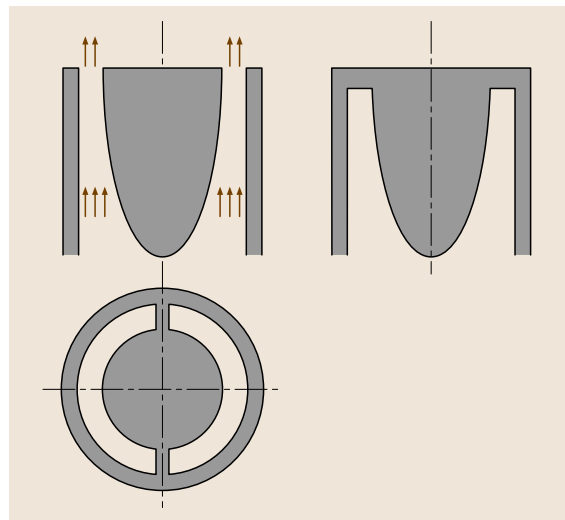


**Fig. 13.13** The plug-jet geometry (after Foss et al.[13.18])

the *near surface*. Also,  $S'_4$  is suggested by the observed streamlines but it is not definitively shown which again represents the difficulty of PIV images being taken in the near-wall region.

The instantaneous realizations of the experiment *also* provide an opportunity to check the PIV data. In these cases, it cannot be expected that the regular (predictable) singular points of Fig. 13.15 will be observed. It is also possible that the software-generated streamlines may give a false image of the velocity field. Hence, it is of value to examine these realizations for their agreement with the appropriate topological constraint.

Figure 13.16a presents a *one-realization image* of this flow field. This figure is exceptionally busy given the intent to allow the multiple singular points to be identified. Also, its lower section has been blocked off given the ambiguities of the PIV data near the plugs' surface. The lower three holes and two seams that are shown bound the overall domain to be investigated. Note that the holes exhibit one-way flow and the seams are tangent to the streamlines. Hence, Fig. 13.16a shows a collapsed sphere with four holes. Again, the Euler characteristic is  $\chi = -2$ .

The terminations of the seams above the plug provide a vector field pattern that mimics that of Fig. 13.12b for the vortex ring analysis. Specifically, there are four  $S'$  values at the terminations of the two seams. Consequently, a correct vector

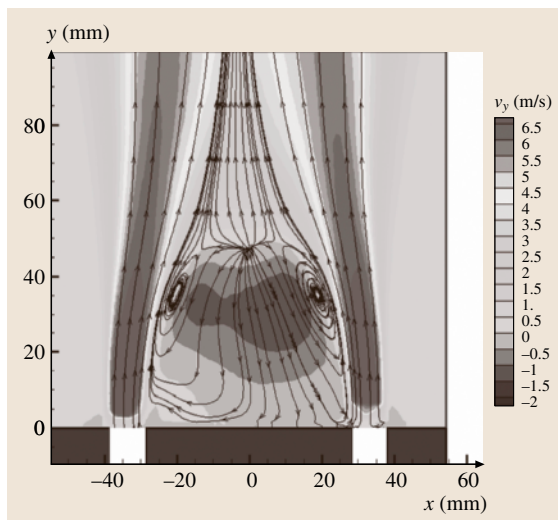


**Fig. 13.14** The average velocity field (1000 realizations) in the center plane perpendicular to the support member of the plug-jet shown in Fig. 13.13. Note,  $x$  and  $y$  dimensions are in mm;  $V_y$  is the vertical velocity magnitude in m/s



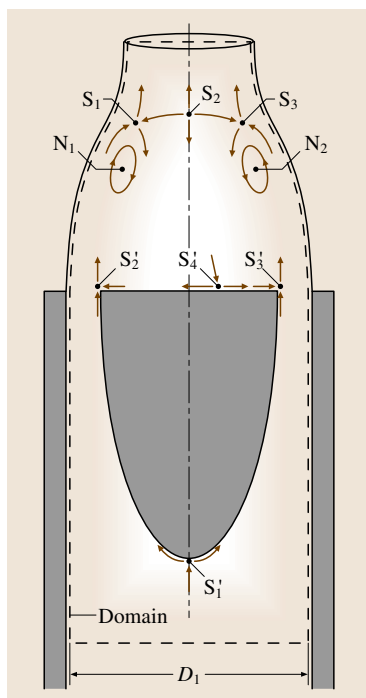


**Fig. 13.15** The collapsed sphere that is used to evaluate the singular points for the flow of Fig. 13.14

field above this lower surface will exhibit one net node.

An efficient protocol, to determine if the overall features of the vector field are correct, is to interrogate the nine subregions, identified in Fig. 13.16b, with the revolving unit vector ([13.1]). This protocol will determine if a net node or saddle exists within a given domain. It is obvious, for example, that both nodes and saddles exist within domain 1. It is, however, not readily apparent if these *cancel in pairs*.

The reader can verify that domains 1–3 and 5–9 exhibit no rotation of the unit vector as it revolves around the perimeter of those domains with the *base* of the vector on the domain boundary and its tip pointed in the direction of the streamline at the base point. In contrast, domain 4 exhibits a clockwise rotation of the unit vector as it executes that traverse. Hence, domain 4 indicates a net node.

The topological constraint is therefore satisfied as

$$\begin{aligned}\chi - 2 &= 2 \sum N + \sum N' - 2 \sum S - \sum S' \\ &= 2(1) + 0 - 0 - 4.\end{aligned}\quad (13.10)$$

Further analysis in the domains will show the self-canceling patterns of equal nodes and saddles. These considerations show that above the *lower cut-off zone* the

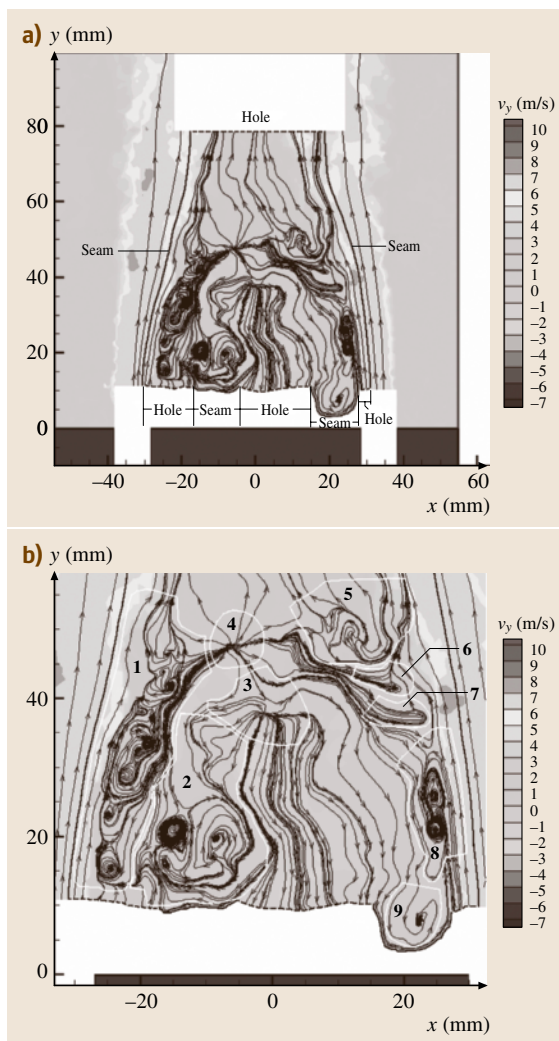


**Fig. 13.16a,b** An instantaneous realization of the velocity field for the plug-jet depicted in Fig. 13.13. (a) The selected domain for which reliable streamlines can be defined. Note, the lower boundary is defined by three holes and two seams at a nominal height of  $x = 0.154D$ . (b) Contour regions

indicated vector field satisfies the topological constraint and the PIV observations are justified.

### 13.2.6 Summary

The surface topology *rule* discussed in this section can ensure that the inferred pattern of singular points does not violate the topological constraints. As shown by the above examples and those of [13.1], the rule can

also be used to extend the experimental observations by the plausible addition of singular points that are not observed. The agreement between multiple surfaces for a given flow is often required to gain confidence that the complete flow field, as typically inferred from incomplete or uncertain observations, is rational.

In addition to these positive attributes, it is appropriate to reiterate that a selected set of singular points could satisfy the rule but not represent the physical flow field. That is, the rule represents a necessary but not

a sufficient constraint on the singular points of the flow field.

This section relies heavily on [13.1] for its basic elements. The examples provided herein are to give the researcher exposure to additional applications of the Rule such that its application in a new problem is readily accomplished. The half-saddles that are required for Fig. 13.11b and Fig. 13.12b (seam 2) were not recognized in [13.1]. Hence, this exposition also adds to the basic considerations covered previously.

## References

- 13.1 J.F. Foss: Surface selections and topological constraint evaluations for flow field analyses, *Exp. Fluids* **37**, 883–898 (2004)
- 13.2 A.E. Perry, M.S. Chong: A description of eddying motions and flow patterns using critical-point concepts, *Ann. Rev. Fluid Mech.* **19**, 125–155 (1987)
- 13.3 A.E. Perry, M.S. Chong: Topology of flow patterns in vortex motions and turbulence, *Appl. Sci. Res.* **55**, 357–374 (1994)
- 13.4 J.C.R. Hunt, C.J. Abell, J.A. Peterka, H. Woo: Kinematical studies of the flows around free or surface-mounted obstacles: applying topology to flow visualization, *J. Fluid Mech.* **86**, 179–200 (1978)
- 13.5 D.G. Bohl: *An experimental study of the near field region of a free jet with passive mixing tabs*, MS Thesis (Michigan State University, East Lansing 1996)
- 13.6 J.N. Koster, U. Müller: Free convection in vertical gaps, *J. Fluid Mech.* **125**, 429 (1982)
- 13.7 G. Zimmermann, P. Ehrhard, U. Müller: Stationäre und Instationäre Konvektion in einer quadratischen Hele-Shaw Zelle, Primärbericht IRB-Nr **507**, 86 (1986)
- 13.8 R. Ruderich, H.H. Fernholz: An experimental investigation of a turbulent shear flow with separation, reverse flow, and reattachment, *J. Fluid Mech.* **163**, 283–322 (1986)
- 13.9 L.J.S. Bradbury, A.H. Khadem: The distortion of a jet by tabs, *J. Fluid Mech.* **70**, 801–813 (1975)
- 13.10 K.B.M.Q. Zaman, M.F. Reeder, M. Samimy: Control of an axisymmetric jet using vortex generators, *Phys. Fluids* **6**, 778–793 (1994)
- 13.11 M.F. Reeder, M. Samimy: The evolution of a jet with vortex-generating tabs: real-time visualization and quantitative measurements, *J. Fluid Mech.* **311**, 73–118 (1996)
- 13.12 D.G. Bohl, J.F. Foss: Near exit plane effects caused by primary and primary-plus-secondary tabs, *AIAA J.* **37**, 192–201 (1999)
- 13.13 C.M. Holland: *Exploratory investigation of the recirculation region and search for coherent motions aft of an axially mounted cone in confined flow*, MS Thesis (Michigan State University, East Lansing 1989)
- 13.14 D. Summer, J.L. Heseltine, O.J.P. Dansereau: Wake structure of a finite circular cylinder of small aspect ratio, *Exp. Fluids* **37**, 720–730 (2004)
- 13.15 C.P. Gendrich, D.G. Bohl, M.M. Koochesfahani: *Whole-field measurements of unsteady separation in a vortex ring/wall interaction*, 28th AIAA Fluid Dynamics Conf. 1997 (AIAA, Reston 1997)
- 13.16 C.-T. Chu, C.-C. Wang, R.-Y. Chang, W.T. Chang: Head-on collision of two coaxial vortex rings: experiment and computation, *J. Fluid Mech.* **296**, 39–71 (1995)
- 13.17 M.M. Koochesfahani: Private communication (2006)
- 13.18 J.F. Foss, R.J. Prevost, K.M. Bade, A. Levasseur: *The velocity field of an annular jet with cross-member*, ASME/JSME Joint Fluids Engineering Conf., FED SM2003-45242 (ASME, New York 2003)